Journal of Alloys and Compounds, Volume 895, Part 2, February 2022, Article number 162735
DOI:10.1016/j.jallcom.2021.162735

β Grain Refinement by Yttrium Addition in Ti-6Al-4V Wire-Arc Additive Manufacturing

*J. R. Kennedy[1,2], A.E Davis[1], A.E. Caballero[3], N. Byres[1], S. Williams[3], E.J. Pickering[1], P.B. Prangnell[1]

[1]University of Manchester, Department of Materials
Manchester, United Kingdom, M13 9PL

[2] Now at Institut Jean Lamour, Campus Artem, 2 allee Andre Guinier, 54011, Nancy, France

[3]Welding Engineering and Laser Processing Centre, Cranfield University
Bedfordshire, United Kingdom, MK43 0PL

(*Corresponding author: jacob.kennedy@univ-lorraine.fr)

ABSTRACT

Wire-Arc Additive Manufacturing (WAAM) of large near-net-shape titanium parts has the potential to reduce costs in aerospace applications. However, with titanium alloys, such as Ti-6Al-4V, conventional WAAM processing conditions generally result in epitaxial solidification from the melt pool fusion boundary, which over many layers can generate coarse cm-scale, <001> // ND fibre textured, columnar β grain structures within the deposited metal. The mechanical anisotropy caused by this coarse primary grain structure cannot be eliminated by subsequent solid-state phase transformations. In order to attempt to refine the size of the solidified β-grains and reduce their strong texture, the growth restriction efficiency of low addition levels of the strongly partitioning element (k = 0.1) yttrium (Y) has been investigated. Less than 0.8 wt% Y was sufficient to reduce the widths of the solidified columnar β grains from 1 - 2 mm to 100 - 300 µm. Y was also found to induce a columnar-to-equiaxed transition (CET) in the latter stages of melt pool solidification, which benefits from a lower liquid thermal gradient and higher solidification velocity. Inter-dendritic segregation of Y was also found to be significant and oxygen scavenging led to the formation of Y_2O_3 particles in the inter-dendritic liquid, with a previously unreported irregular eutectic morphology. High-resolution EBSD analysis showed these particles exhibited specific orientation relationships with the solidified β grains, which were confirmed experimentally.

KEYWORDS

Additive manufacturing, Grain refinement, Titanium, Ti64, WAAM

Published by Elsevier. This is the Author Accepted Manuscript issued with: Creative Commons Attribution Non-Commercial No Derivatives License (CC:BY:NC:ND 4.0).
The final published version (version of record) is available online at DOI:10.1016/j.jallcom.2021.162735. Please refer to any applicable publisher terms of use.

1.0 Introduction

Titanium (Ti) alloys are known for their excellent specific strength, as well as their high corrosion and oxidation resistance [1] and, as such, are one of the most important metallurgical systems used in aerospace applications [2]. However, the production of conventional wrought Ti components (e.g. forgings) is associated with high costs due to their challenging processing and machining requirements [3]. A potential solution, now being widely investigated, is the nearer-to-net-shape production of Ti airframe components by directed energy deposition (DED) high rate Additive Manufacturing (AM) [4] [5]. Many AM technologies are currently being developed for applications involving the alloy Ti-6Al-4V (Ti64) [6–8], as it is the most commonly used Ti material in aerospace. Of these processes, Wire Arc Additive Manufacturing (WAAM) is particularly suited to free-form manufacture of large-scale components because of its high deposition rate and low capital equipment costs [9].

WAAM is a layer-wise AM process that builds up parts by depositing material through melting a metallic wire fed into a translated melt pool, formed by a gas shielded plasma-arc heat source [10]. Although WAAM has a high deposition rate, with alloys like Ti64 the solidification conditions dictated by the larger heat source and moving melt pool commonly result in coarse columnar β grains forming in the deposited metal, that can have a negative effect on its properties and, in particular, create anisotropy in components[11]. The prevalence of coarse columnar grain structures in Ti-64 AM deposits is related to the metallurgy of the Ti-Al-V system, which exhibits low partitioning of Al and V, limiting the potential for constitutional undercooling at the solidification front. This behaviour is exacerbated by the positive thermal gradient present in the liquid (G_{L}) with a heated and translated melt pool [12]. With high translation rates, which leads to a high solidification front velocity (v), low values of G_{L}/v can still be achieved in a moving melt-pool near its centreline [13]. Nevertheless, the low level of solidification front solute partitioning found in Ti64, and a lack of efficient nucleants, leads to the β grains solidifying epitaxially from the fusion boundary with little to no nucleation ahead of the solidification front across the entire melt-pool. These conditions allow continued growth up through multiple added layers, which selects favourably orientated grains with a common preferred <001> growth direction [14,15]. Although on cooling to room temperature Ti64 transforms from the as-solidified β grain structure ~ 90% lamellar α, the α variants that form inherit a texture from their parent β grains due to the Burgers Orientation Relationship (BOR) [16]. Subsequent thermal cycling through the β transus cannot remove this inherited texture. When combined with the plastic heterogeneity promoted by the formation of single variant α colonies on the β grain boundaries, this can cause significant anisotropy and unwanted scatter in mechanical properties, such as ductility and fatigue crack growth rates [17] .

In order to improve the negative effects of a coarse β primary grain structure on the consistency of the mechanical performance of AM components, different methods have been implemented to refine the columnar grains formed during solidification. One such method exploits inter-pass deformation, introduced by techniques such as rolling [18] or peening [19], to deform the surface of each deposited layer before the next layer is applied. When combined with reheating by the heat source through the β transus during subsequent deposition passes, this results in β recrystallization and refinement of the columnar grain structure [20]. This method is attractive as there is no change in the base alloy composition, so conventional recycling streams

can still be maintained, but requires an additional processing step and is challenging to apply to more complex geometries, which slows production time and increases costs.

Grain refinement is also possible by metallurgical means during solidification, through changing the alloy composition, by the addition of heterogeneous nucleation sites (inoculation) and/or the addition of solutal growth restrictors [21]. A number of inoculant systems have been trialled in AM with Ti64 with varying degrees of success [22–26], but have the disadvantage that they involve the introduction of hard second phase particles into a high performance material, which can provide sites for damage nucleation [27]. Solutal growth restrictors are elements that segregate strongly in the liquid ahead of the solidification front, modifying the constitutional undercooling encountered by the growing solid. This restricts the growth of the solid nuclei, as well as both modifying the perturbation wave length [28] and changing the dendrite tip radius [29,30], and increasing constitutional super cooling, thus providing more opportunity for nucleation ahead of the solid-liquid interface. The overall effect of their addition is thus to reduce the average size of the grains that form during solidification. But, without favourable solidification conditions and the presence of efficient inoculant particles in the melt that are effective at low undercoolings (< 3 K), this does not necessarily promote a columnar to equiaxed transition (CET) [31–35]. The application of solutal growth restriction to refining grain structures in AM would clearly be a more attractive option if it was successful with; i) the low addition levels of new elements that ii) do not produce any unwanted side effects, such as the generation of brittle second phases.

Growth restriction in an alloy can be rationalised in terms of the potential for partitioning at the solidification front [36], by the restriction factor, Q, given by:

$$Q = m(k-1)C_0 \qquad \text{(eq – 1)}$$

Where; m is the liquidus slope, k is the partition coffcient, and C_0 is the average solute content in the melt. The goal of this approach is to change the conditions sufficiently at the solidification front such that the CET is surpassed, cutting off the growth of the columnar grains [21]. A table of k, and thus potential Q values for potential growth restricting elements in Ti alloys has been previously compiled by Bermingham et.al. [31]. Unfortunately, most metallic elements that do not promote intermetallic compounds with Ti from extensive solid solutions and do not partition strongly, leading to low 'Q' values. Several metalloid elements, that do have low values of k, such as the Be [31], B [37], and Si [38] and rare-earth addition La [22] elements have been investigated as growth restrictors in Ti during AM. However, such elements tend to form undesirable brittle phases (e.g. TiB_2 [39]) reducing fracture toughness. Less effective elements like Fe (k = 0.38) have also been investigated, but they require high concentrations (3 wt.%) to even induce mixed columnar/equiaxed structures, which means developing an entirely new alloy [40]. An alternative addition that theoretically might be expected to show promise for solutal growth restriction, that has not been widely studied in AM, is Yttrium (Y). Similar to B, Y has a very low partition coefficient with Ti, equivalent to $k \sim$ 0.1 [31] and, although it has low solid-solubility in titanium (max $\sim$ 2 wt%), in a binary Ti-Y system Y does not produce any intermetallic compounds and precipitates as elemental particles [41].

Small Y additions are, however, known to have a several important effects on Ti alloys, both positive and negative, which are highly dependent on the alloy composition and processing route. [42]. In casting, Y additions to Ti64 have already been shown to result in an order of magnitude refinement of the β grain size [35]. Furthermore, Y has been observed to refine the grain structure of Ti during arc welding, as well as change the fluid flow and bead morphology [43]. This grain refining ability of Y has been attributed to the beneficial effect of Y on growth restriction, but also to the possibility of heterogeneous nucleation occurring on Y_2O_3 (yttria) particles generated in the melt during solidification [44], which are formed as Y scavenges O from Ti [45]. However, this has been found to be insufficient to induce a CET and modelling indicates that yttria particles less than 30 μm in diameter have a tendency to melt during AM processing [46]. While these oxide nano-particles can increase strength [46], they also decrease ductility, especially at high (2 wt% Y) addition levels [47]. Y has also been investigated as an alloying element with potential for providing yttria (Y_2O_3) dispersoid hardening in powder metallurgy Ti alloys since the 1960s, where in some cases the addition of Y can increase ductility, by gettering O from the matrix [48], or by modifying the composition of other precipitates, such as silicides [49]. The yttria particles also strongly interact with grain boundaries in Ti alloys by providing a strong Zener pinning force and are known to be highly effective at preventing the rapid grain growth that normally occurs during β heat treatments [50]. Such an additional benefit could also be exploited in AM, as even if grain refinement is successful, re-heating above the β-transus when each new track is deposited can cause significant grain growth [51].

Thus, although there are known beneficial effects from making small Y additions to Ti alloys that could help control the primary β grain size in WAAM, the interactions are complex and currently not well understood, particularly in the context of high deposition rate AM processes. This paper therefore aims to investigate in more depth the potential for Y as a grain refining addition to Ti64, during a high deposition rate wire-AM process. To this end, experiments have been conducted whereby WAAM Ti64 test deposits, produced under standard deposition conditions, were doped with fine Y powder and the resultant grain structures, β texture and microsegregation of Y and its associated phases, were investigated in detail using a combination of electron microscopy techniques.

2.0 Materials and Methods

A simple methodology was employed to add Y to the melt pool, whereby Y powder was premixed with a polyurethane adhesive and then applied as a thin coating to the top of each new deposited layer. The minimum amount of adhesive (polyurethane) was used to prevent the powder being blown off the deposit by the plasma torch (a similar method has been employed previously [26,52] and by Bermingham et al. [23]). The 99.5% purity Y powder used in the investigation was sourced from Sigma Aldrich with a 40-mesh particle size (< 420 μm). To minimise oxidation, the container was unsealed in a glove box under Ar when mixed with the polyurethane adhesive. This mixture was re-sealed in the glovebox before transport to the low oxygen (~800ppm) WAAM enclosure for deposition, using a plasma transferred arc (PTA) process, the same day. A single melt track-wide wall was then built 10 layers high using only Ti64 wire, to attempt to first establish a typical coarse starting β grain structure, after which a further 10 layers were added with the addition of the Y particle loaded polyurethane coating between each layer. An identical control sample was also built using only the adhesive in the top 10 layers, without Y,

as well as a sample only containing Ti64. The bulk compositions of the upper half of the three deposits are provided in Table 1. The WAAM deposition parameters are provided in Table 2 and a schematic of the sample geometry can be found in Figure 1. The heat source travel direction was kept constant, as shown in Figure 1, where the three sectioning positions used are also depicted: i) 40 mm in from the start position (front section), ii) the wall centre (transverse section), and iii) 40 mm before the end position (back section). The sample reference frame is also shown; where ND is the layer normal direction, WD the direction along the wall and heat source travel direction, and TD is the transverse direction normal to the wall faces. Identical parameters were used in previous work [26,52] where comparable baseline results for samples built using only Ti64, as well as just with a polyurethane coating (Ti64-P) can be found. This showed that when the polyurethane adhesive was used alone it did slightly increase the C content of the deposit, but this had a minimal effect on the β grain structure [26].

Table 1: Bulk compositions (wt%) measured for the top 10 layers of each build

Wt%	**Ti**	**Al**	**V**	**Fe**	**O**	**N**	**C**	**Y**
Ti64 [26]	89.43	6.22	3.95	0.20	0.17	0.01	0.02	0
Ti64-P [26]	89.51	6.13	3.95	0.19	0.16	0.01	0.05	0
Ti64-Y	88.60	6.11	3.90	0.21	0.22	0.02	0.07	0.76

Table 2 WAAM deposition parameters

WAAM build parameters	
Travel Speed	5 (mm s^{-1})
Current	160 (A)
Wire Diameter	1.2 (mm)
Layer Height	~1.1 (mm)
Plasma Gas Flow	0.013 (L s^{-1})

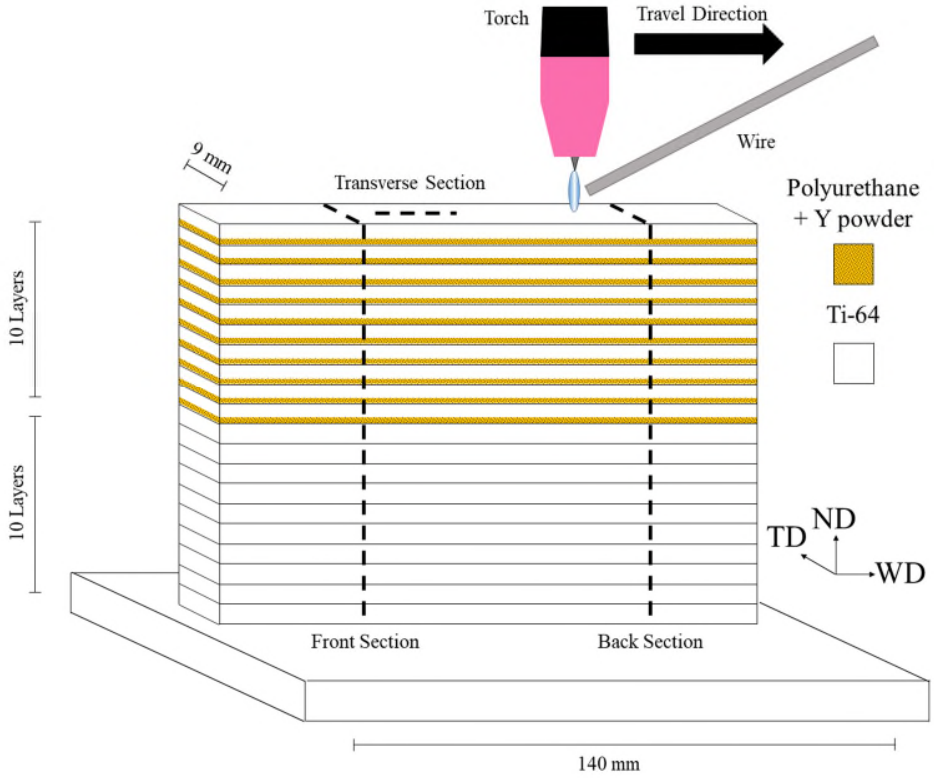

Figure 1: Schematic of the test samples studied, which were built as 20-layer high, single pass wide, linear walls, with a constant heat source travel direction (shown). The sections used for microstructure and texture analysis are indicated.

The test samples were sectioned at the positions shown in **Error! Reference source not found.** and metallographically prepared by grinding with SiC paper, followed by a finishing polish using a 0.25 µm OPS (colloidal silica) suspension. To investigate the bulk β grain size and texture of each test build, large area α phase EBSD orientation maps of the sample cross sections were acquired with an FEI Sirion FEG-SEM operated at 20 kV, equipped with an OI Nordlys Nano EBSD camera. Higher resolution large area EBSD/EDX maps were acquired with a Tescan Mira3 FEG-SEM using an OI Xmax SDD-EDX detector and an OI Symmetry CMOS EBSD camera. High resolution investigations of the microstructure and second phase particles were carried out using an FEI Magellan equipped with an OI Xmax SDD-EDX detector and OI Nordlys Nano EBSD camera.

The primary WAAM β-grain structure that develops during solidification is very difficult to directly index by EBSD at room temperature in Ti64 because of the fine α transformation microstructure that forms during cooling. The parent β grain structures were therefore reconstructed from α EBSD orientation maps using the methodology of Davies and Wynne [16,53], which is based on exploiting the BOR (i.e. $\{110\}_\beta // \{0001\}_\alpha$ and $<111>_\beta // <11\bar{2}0>_\alpha$) to calculate the most probable parent β orientation from neighbouring α variants.

3.0 Results

In order to first better understand the phases theoretically expected to form in the Ti-6Al-4V-Y-O system, Scheil-Gulliver solidification calculations were performed using ThermoCalc2019a software, with the TCTI2.0 database, using the composition of the sample deposited, which was measured to contain 0.76 wt.% Y and 0.22 wt.% O (Table 1). The results of these calculations are shown in Figure 2. The predicted primary solidification phase is β, and with the oxygen level measured in the build included (0.22 wt. %), Y is expected to precipitate from the melt directly as yttria (Y_2O_3), due to its high affinity for oxygen (ΔG = -1.8 kJ mol^{-1}). However, this does not happen until there has first been considerable enrichment in the liquid of both yttrium and oxygen due to melt partitioning and yttria is only predicted to start to form when the last 3% of liquid remains. It should be noted that due to the presence of oxygen, and to a lesser extent the other alloying elements, the β phase does not reach the Y saturation level of 3.7 wt% predicted in the binary Y-Ti phase diagram [41] and only reaches a maximum of 0.1 wt% Y before yttria begins precipitating. The fully solidified material was calculated to contain 0.4 wt% of yttria (Y_2O_3), with no elemental Y phase predicted. These thermodynamic calculations therefore show that an elemental Y phase would not be expected to form from the melt pool during WAAM deposition, unless the oxygen content was substantially reduced and thus only yttria is expected to be seen in the deposits.

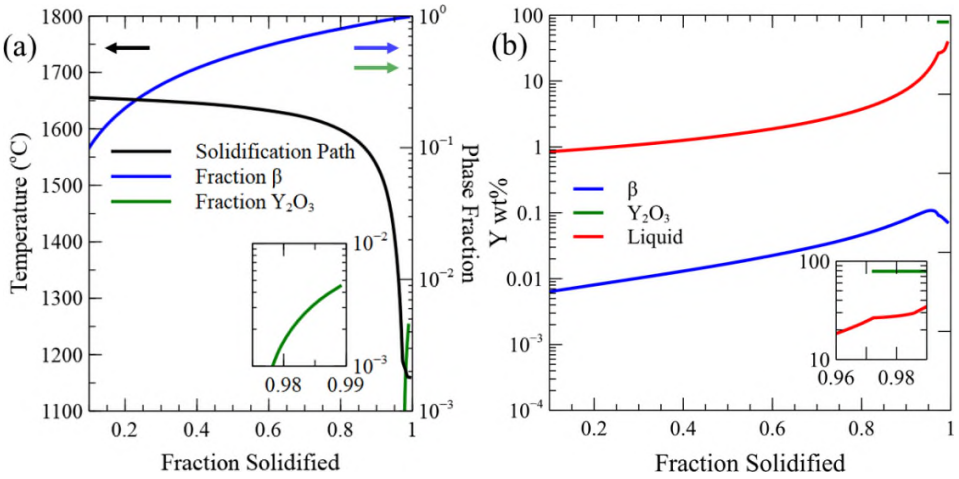

Figure 2: Scheil-Guliver solidification calculations produced with ThermoCalc, using the measured deposit compositions listed in Table 1 showing the predicted (a) solid fraction with temperature on a linear scale and the relative proportions of β and yttria phases vs fraction solid on a log scale, to highlight the small fraction of and yttria formed in the latter stages of solidification (wt%) of the solidified phase and (b) Y composition in each phase present as solidification progresses. Inset, the scale has been increased to focus on the latter stages of solidification

4.1 Grain Structure and Texture

Large area reconstructed β EBSD orientation maps produced across the full ND-TD WAAM test-samples' cross-sections are provided in Figure 3. In Figures (a)-(c) the top 10 layers were built with Y additions and the bottom layers were deposited with just Ti64 wire. The control in Figure 3 (d) was built entirely with Ti64 wire and no Y addition. The ND-TD cross section maps in (a) and (b) were taken from the start (front section in Figure 1) and end position (rear section in Figure

1). An ND-WD section along the wall centre line (transverse section in Figure 1) is also shown in (c). The bottom part of all the sections can be seen to consist of a typical WAAM microstructure [8,15,54], where a coarse β grain structure is in the process of becoming established. However, it appears the deposition of ten layers was too few to develop a true steady-state, before adding the Y powder and the mm-scale columnar grains typically seen in taller samples (e.g. [14,15]) were still starting to develop in the walls' bottom sections. The more typical columnar grain structure found in large WAAM parts can be seen continue to develop in the 20 layer high Ti64 control sample, shown in Figure 3 (d). A distinct transition between the bottom sections, which contained just Ti64, and the top layers with Y additions can, however, still be observed in the reconstructed EBSD maps - where the grain structure changed significantly. Comparison of Figures 3 (a) –(c) with (d) clearly shows that in the top ten layers a much finer (in terms of grain width) columnar grain structure developed in the Y doped sample. In addition, a 'casing' of fine equiaxed grains can be seen in the Y containing sample close to the top and side surfaces of the deposit, which is not present in the baseline sample.

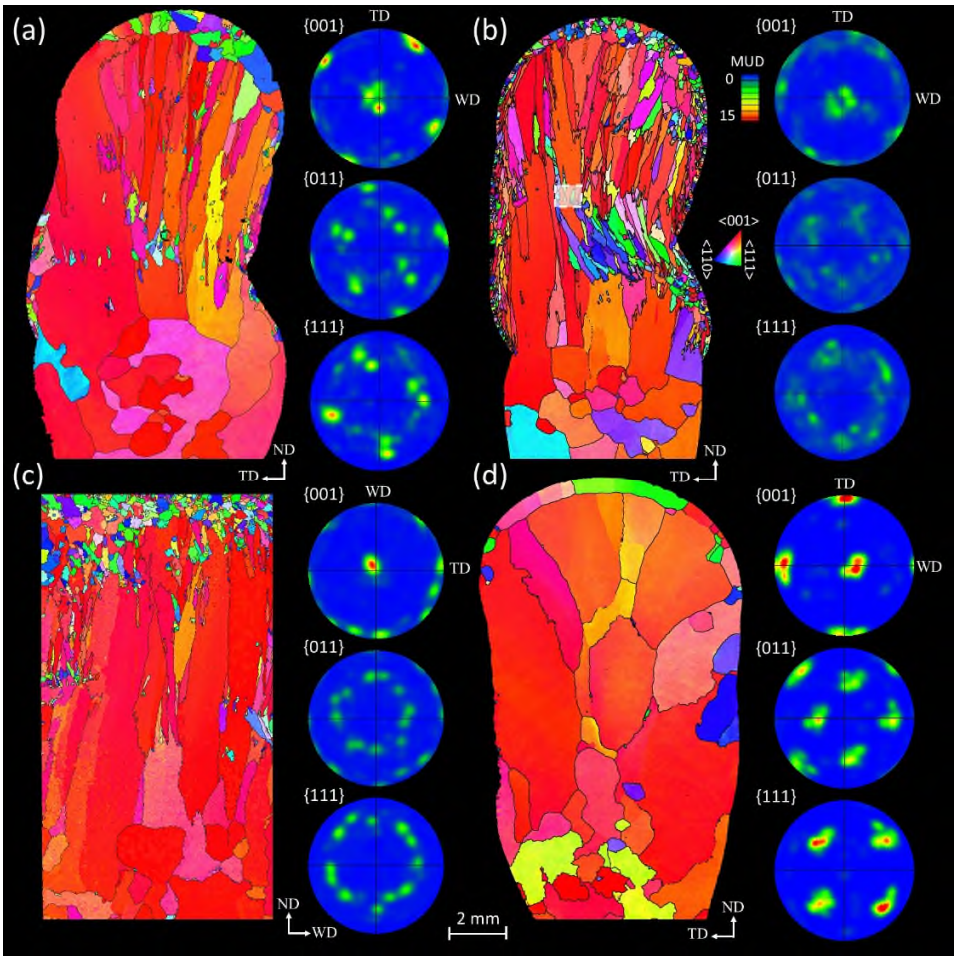

Figure 3: Large area reconstructed IPF-ND β EBSD orientation maps from the test-sample sections, indicated in Figure 1, showing the transition to the top ten layers added with Y additions from: (a) the front of the wall; (b) the rear of the wall (c) and a transverse central section; (d) shows the

control Ti64 wall deposited without any Y additions. The pole figures indicate the respective textures obtained from the top ten layers.

In Figure 4 the change in average columnar grain widths, measured across the TD from the reconstructed β EBSD maps in the ND-TD sections taken from the maps in Figure 3, are plotted as a function of build height (ND). The fine grains seen in the surface regions were disregarded from this analysis as they were not representative of the bulk microstructure. It can be seen that in the bottom section of each sample, where no Y was added, the grain widths were similar for all the samples and were all in the range of 900 - 980 µm. In the control sample, with increasing wall height, the grain width then increased significantly to ~ 1500 µm before reducing again in the top layers of the build. This reduction is likely to be due to the final layers being exposed to fewer deposition passes, and thus less reheating and grain growth. In contrast, in the top section of the Y doped deposit the average grain widths were measured to be in a range of ~200 µm to ~300 µm, which represents a significant reduction. There is also no reduction in the top deposited layers when compared to those produced with more reheating steps, indicating that the yttria particles may be hampering grain growth [50]. Additional data is included in Figure 4 from the control sample that was deposited in parallel experiments (EBSD and pole figures available in [26]), just using the adhesive (Ti64-P). The results for this build show no evidence of a reduced grain size arising from the small quantities of carbon entering the melt from the adhesive (full details of this specimen can be found in Ref. [26]). The scatter in the data for the Y free deposited layers reflects variability caused by the few coarse β grains present across the width (in TD) of the small trial samples.

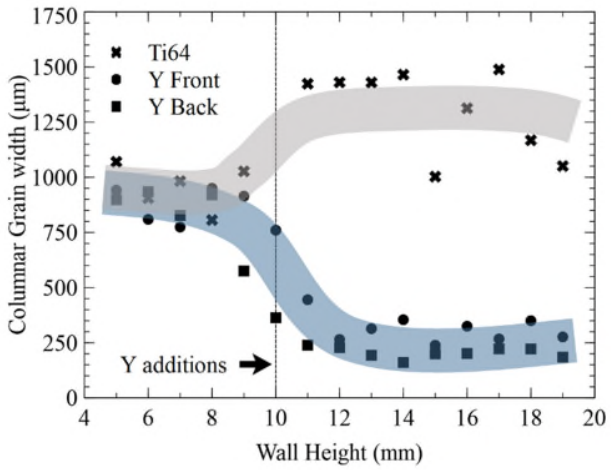

Figure 4: The average change in width of the columnar β grains with build height in the Y containing and Y free control sample, measured by the linear intercept method in TD on ND-TD cross sections.

Below the Y-containing layers, the β microstructure consisted of coarse mm-scale grains oriented with a common <100> direction aligned close to ND. This texture can also be seen in ref [26] and is depicted in the pole figures for the baseline sample in Figure 3 (d), which is dominated by the presence of a small number of similarly orientated grains that show a close to $\{001\}_{ND}$ $<010>_{WD,}$ or 'cube', alignment. Although, there are too few grains in these small test samples to reliably compare the textures, it can be observed in the pole figures taken from the 3 sections

obtained from the refined top half of the Y doped sample (Figures 3 (a) - (c)) that the finer columnar grains have still grown with a similar texture, involving a common preferred <001> growth direction, but there is now a greater spread in the fibre around <001>//ND. The texture is also weaker overall, especially in the case of the rear section (Figure 3(c)) which contains more grains that are orientated away from the <001> fibre.

4.2 Y distribution within the builds

In the top layers of the test sample, where low concentrations of Y powder had been added to the melt pool, small inter-dendritically distributed Y-bearing particles were observed in bands by SEM backscattered electron (BSE) imaging, as shown in Figure 5. A number of pores were also located along the same bands, which can be seen in Figure 5 to be concentrated in the inter-dendritic regions associated with the particles. The high porosity seen in the top part of the build with Y additions can be partly explained by yttria particles being pulled out during polishing. However, the higher magnification views of the pore morphologies in Figure 5b suggest that these are more likely to be caused by gas, or, shrinkage pores. Such porosity is not normally seen in conventional Ti64 WAAM builds produced under identical conditions, which contain virtually no gas pores [55].

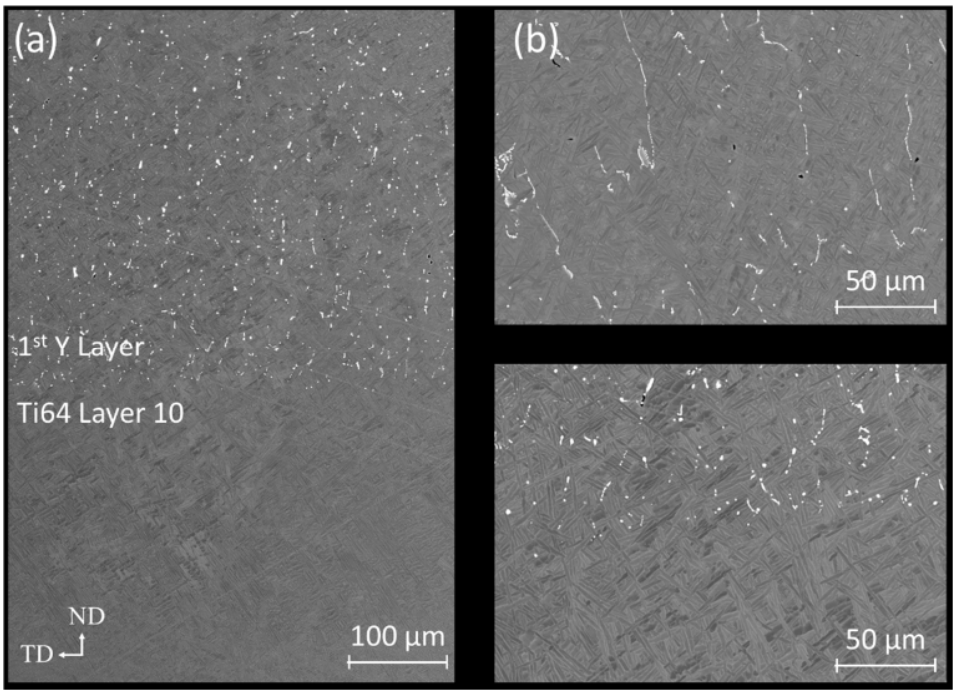

Figure 5: BSE micrographs (a) showing the interface between the Ti64 base and the 1st layer of Y additions (b) higher resolution micrographs of Y bearing particles in the layers containing Y (top), note the dark regions (porosity) collocated in a linear fashion with the bright Y bearing particles, and interface region of the first Y containing layer (bottom).

Further investigation of these small particles at higher magnification revealed them to be in the range of ~ 0.1 – 2 µm in size, when imaged using conventional polished 2D cross sections.

Their equivalent circular radius (r) size distribution, obtained from > 5000 particles, is provided in Figure 6, which shows that the majority of the particles were less than 1 μm in size, with a median radius of 240 nm and average of 320 nm, and an average area fraction of ~0.8%.

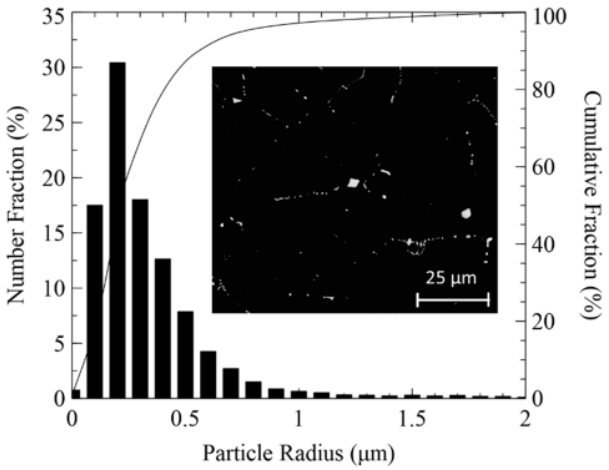

Figure 6: Size distributions of Y bearing particles measured by SEM imaging of 2D metallographic sections with inset that shows an example BSE image used for measurement.

On further investigation by high resolution EDX/EBSD, it was found that the Y rich particles could be nearly all indexed as Y_2O_3 (yttria) (Figure 7b). By comparison of the reconstructed primary β grain structure with larger area EBSD/EDS phase maps (Figure 7a-b), it was evident that the particles were preferentially aligned in inter-dendritic bands along the same direction as the columnar β grains' main <100> growth direction. This was especially apparent in the first layer added with a Y addition, where Y_2O_3 particles were seen to appear from the base of the fusion boundary (Figure 5a).

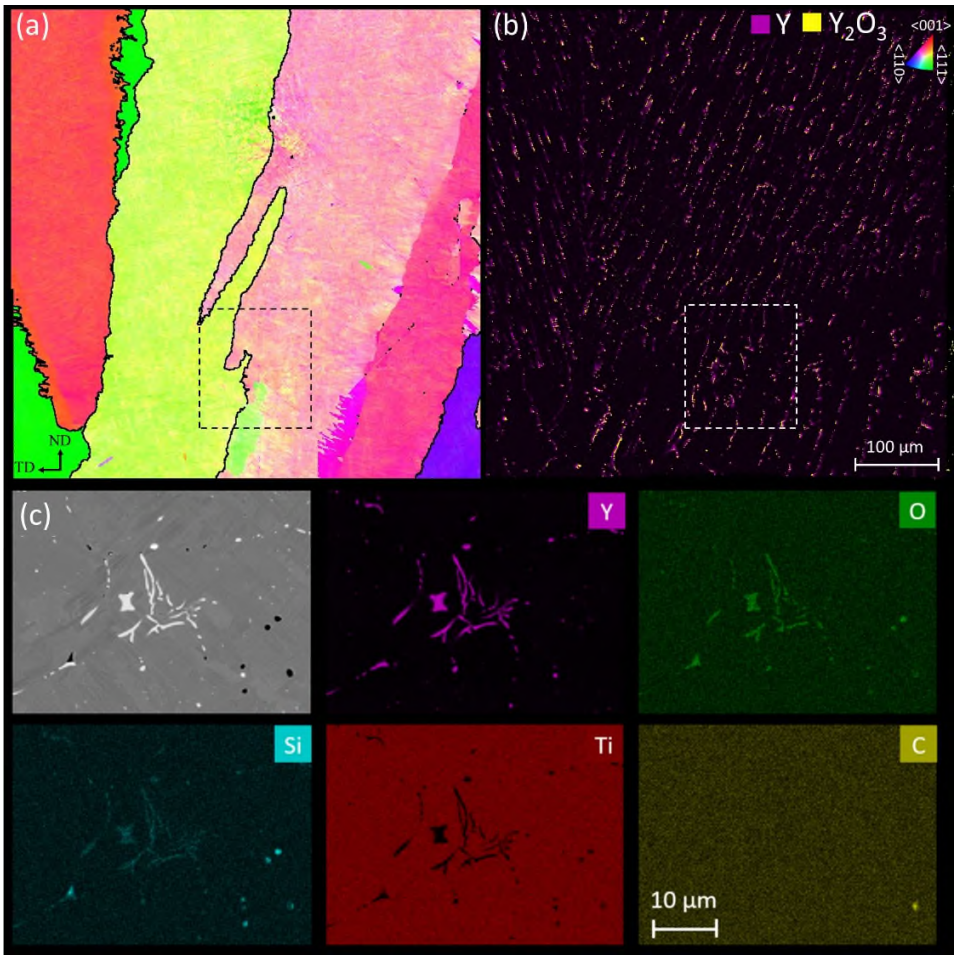

Figure 7: a) EBSD IPF//ND orientation map showing the reconstructed β grain structure and a corresponding large area (b) Y_2O_3 / Y EBSD/EDS phase map (see discussion). The dashed box indicates the area analysed at higher magnification in Figure 9. (c) Higher resolution BSE image and EDS maps of a typical particle cluster.

Higher magnification EDS maps (Figure **7**c) revealed that the particles did not contain significant Ti nor any C contamination from the polyurethane adhesive. At this resolution, EDS mapping did, however, show an increased O and Si concentration in the particles. Si was also located in the pores, probably mainly as a contaminant from sample preparation (i.e. OPS polishing). Closer investigation of the BSE micrographs showed that the bright particles were often co-located with pores, of varying sizes. In some cases the pores encompassed the entire perimeter of the particles. While some pores appeared without Y bearing particles, and this could have been due to particle pullout during metallographic preparation, the majority of larger particles were found to be in contact with a pore. There was also a subset of much smaller, sub-micron, low aspect ratio Y particles, which appeared well dispersed without any associated porosity. These pores may negatively affect the mechanical properties of the alloy [56].

5.0 Discussion

5.1 β grain structure refinement

In WAAM with Ti64, under standard processing conditions, normally very little grain nucleation occurs ahead of the solidification front [57]. Below each new melt track, as the heat source approaches, full transformation to β takes place [54] which results in reformation of the prior-β grain structure that solidified in the previous layer. The reformed β grains can also coarsen due to the high temperatures reached in the β phase field and a lack of strong solute drag, or second phase pinning effects in Ti64 [31], although this is most significant when the β grain structure is small. Solidification then occurs by epitaxial growth from the reformed and coarsened β grains present below the fusion boundary. This gives rise to continuous growth of columnar grains through multiple added layers. As there is no new nucleation, when combined with competitive selection of grains preferentially aligned with the thermal gradient at the solidification front, after multiple layers this leads to the development of a grain structure comprised of very coarse columnar grains with a common <001> direction parallel to the average solidification direction. This alignment direction is determined by the melt pool profile and deposition strategy and with a constant heat source translation direction is generally tilted slightly away from ND towards WD [25,57–59].

The addition of a low concentration of Y to the melt pool in the WAAM process led to several notable effects on the microstructure of the test samples. Overall, the strong influence of Y is related to its low partition coefficient (k = 0.1), which provides a larger solidification temperature range and a wider mushy zone at the solidification front, with more developed dendrites, and greater growth restriction [31,35,60]. No evidence of any surviving Y particles from the original powder was found in the deposited material, in any of the samples investigated, which indicates that the powder fully dissolved in the melt pool where it was dispersed by convective fluid flow [61]. Given the short melt contact times [62], the efficient dissolution of any melt-pool additive is important in an AM process and for Y this can be attributed to its lower melting point (1522 °C) relative to the solvent Ti64 alloy [41], combined with its full solubility in the liquid phase.

It is apparent from Figures 3 - 4 that the addition of low concentrations of Y (< 0.8 wt. %) to the liquid resulted in a large reduction in the scale of the primary β grain structure that forms on solidification within the WAAM samples. This did not, though, result in a CET being seen across the multiple layers produced with Y additions, although it was observed to occur at the top of the final deposited layer. It is also apparent from the abrupt transition in the refined columnar grain widths seen in Figures 3 and 4 that some limited grain nucleation must have occurred when Y was first added. The Y concentration in the first few layers deposited with the added powder will have also been lower than in subsequent layers, because of dilution by the Y free base layer. For example, in the WAAM process the added material is typically diluted by ~ 50-70% due to re-melting [63]. In Figure 3 it can similarly be seen that the columnar grain width fell to reach a steady state lower level over ~ 3-4 added layers, as the dilution reduced with each subsequent layer [64].

From the compositions shown in Table 1, it can be estimated that there was a slight excess of O (0.6 at.%) present in the final build compared to Y (0.4 at.%), relative to that required by Y_2O_3

stoichiometry. ThermoCalc also predicted 0.4 wt% Yttria in the final deposit. This indicates that enough O was present for the added Y to mainly form yttria during the latter stages of solidification (see below). It is thus likely that the 'free' Y present in the liquid that could act as a solute growth restrictor was mainly that added with each new layer, while the Y in the previous layers remained trapped as yttria, and was therefore effectively diluted by ~50% through remelting. However, due to remelting some of the high melting point yttria particles present in the previous layer would also be expected to be released into the melt pool and could potentially also act as heterogeneous grain nuclei.

Higher resolution EBSD analysis of the top, final deposited layer, taken from the ND/WD transverse section, shown in Figure 8, confirms that at the melt-track centreline the top ~1 mm was composed of randomly orientated, fine-equiaxed, grains and therefore the final added layer did exhibit a CET during solidification. Consistent with this observation, in an alloy that exhibits sufficient solute partitioning, the columnar-equiaxed transition is expected to be most likely to occur at the top-centreline of the melt pool where the last liquid freezes and the G_{L}/v ratio is lowest, whereas G_{L}/v is greatest at the fusion boundary [13]. However, in an AM process this is also the region most likely to be remelted during the addition of the next added layer. Using conventional deposition parameters in this sample along with the addition of Y did induce a CET during solidification in the most favourable portion of the melt pool, in most of the sample this refined region would have been remelted during deposition of each subsequent layer. It is thus apparent that Y did increase the process window where equiaxed grain structures can be achieved and changing the conditions to reduce G_{L}/v, by increasing the translation rate and cooling the melt pool (i.e. by reducing the power per unit volume of wire), or reducing the remelt depth, would be expected to have resulted in more extensive grain refinement.

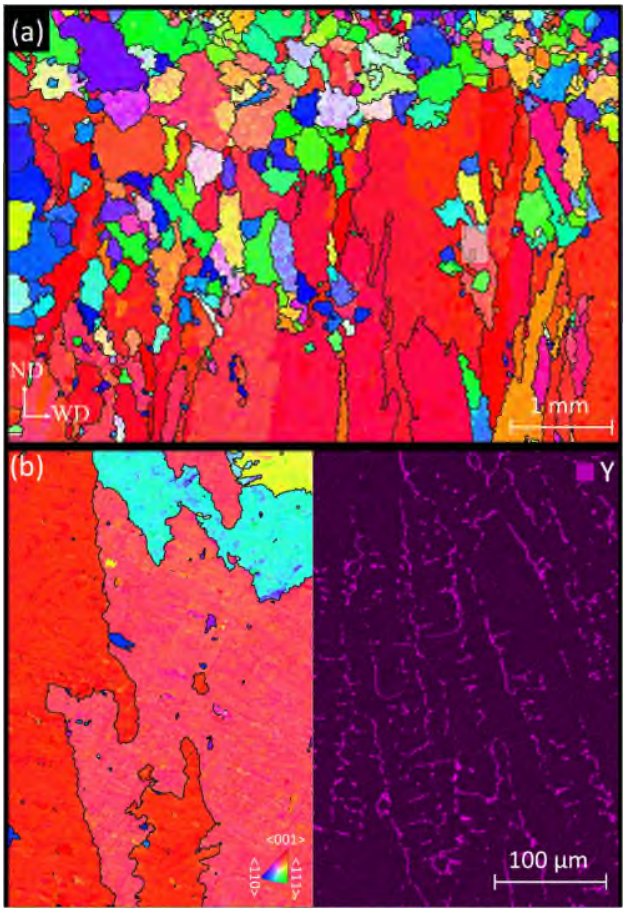

Figure 8: EBSD IPF||ND reconstructed β map of (a) the top of the last deposited layer, alongside (b) enlarged Y EBSD and Y EDS map for columnar type solidification regime.

5.2 Y-bearing particles

The sample layers produced with the Y powder contained Y bearing particles, distributed inter-dendritically within the β grains. The strong tendency for Y to concentrate in the inter-dendritic regions was expected from its low partition coefficient (which is why Y was selected for its high growth restriction efficiency [31,44]). Although some of these particles were too small to identify by EBSD, where the patterns could be indexed they were found to match well with the FCC $Ia\bar{3}$ crystal structure for Y_2O_3. With the oxygen concentrations measured in the sample, the ThermoCalc calculations also predicted yttria would be the most stable phase to appear during solidification in the enriched inter-dendritic liquid (Figure 2b) and this phase was consequently found to delineate the dendrite boundaries of the directionally solidified β grains (Figure 8b). Although the samples studied in this work were built under Ar in a low O chamber (600 ppm) the O level measured was higher than normally found in WAAM builds ~ 0.1-2 wt.% [26], which indicates some additional O may have entered the melt-pool from the Y powder, despite efforts to minimize this, as a similar increase has not been seen in builds produced with different powder under identical conditions [26,52]. The possibility that, as well as Y performing as a growth restricting element, Y_2O_3 - yttria particles entering the liquid can act as an inoculant [44], should therefore also be considered. Yttria has a very high melting point of 2,425 °C and particles that

form in the interdendritic liquid will be released into the melt-pool during the next pass when re-melting occurs, and may then be able to act as a source of grain nucleants.

In Figure 7 the two large β grain orientations present in the reconstructed EBSD map show that solidification occurred dendritically, with mainly <100> || ND primary arms, and the Y_2O_3 particles were strongly concentrated in the inter-dendritic regions [31]. An additional, high resolution IPF map of the indexed yttria particles is provided Figure 9. Interestingly, this reveals that rather than having random orientations the Y_2O_3 particles appear to be in clusters with similar common crystal alignment. When checked using specific pole figures (Figures 9b), the particles within such clusters were found to frequently have virtually the same orientation. For example, in the cluster shown enlarged in Figure 9b, only two distinct Y_2O_3 orientations can be seen: green at the top and purple at the bottom. It can further be noted in Figure 9b that, while the purple particle 'cluster' at the bottom has been sectioned as contiguous, the green 'cluster' is made up of multiple discrete 'particles' that also all have nearly identical crystallographic orientations. It is thus apparent that the separate particles seen in the 2D sections were in fact inter-connected out of plane and consist of larger, complex-branched, particles with a similar 'skeletal', shape to that of the purple particle seen at the bottom of Figure 9b. This morphology is comparable to that of irregular eutectic microstructures found in other alloy systems produced by a faceting (non-metal) and non-faceting (metal) phase (e.g. Al- Si or Al-Mg_2Si [65])

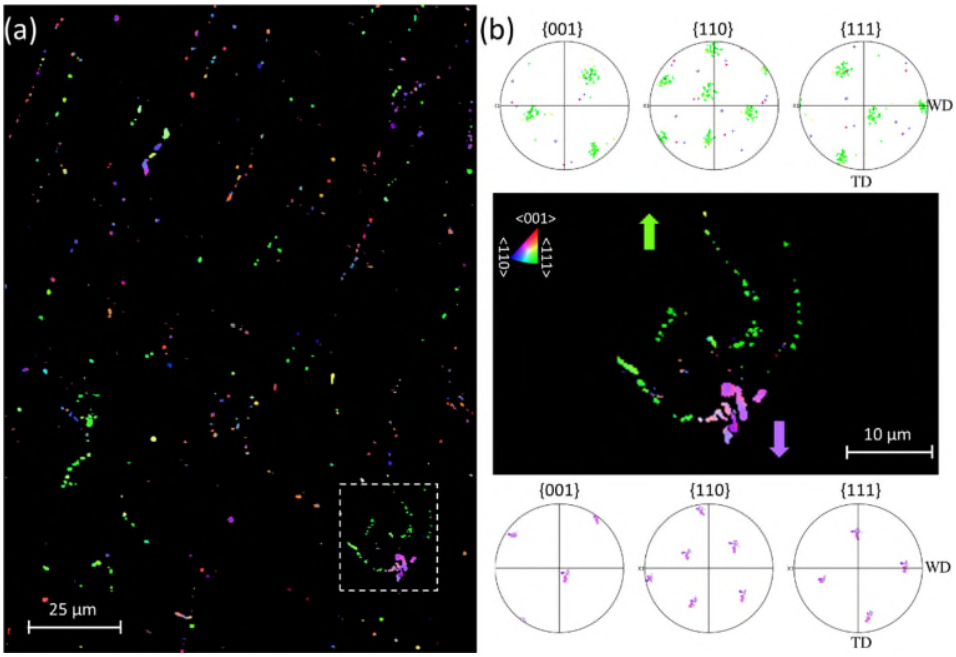

Figure 9: High resolution SEM-EBSD Characterization of Y bearing particles, obtained with a 0.2 µm step size – (a) showing a larger area with Y_2O_3 IPF ||ND (b) high magnification views of a typical cluster of particles with orientations of the Y_2O_3 phase in IPF ||ND, with accompanying pole figures.

As shown in Figure 7 for the steady state Y doped region of the wall, the yttria particles are distributed not only along β grain boundaries but also within β grains. It is also evident from EBSD orientation mapping that while the yttria delineates individual cells or dendrites these grow in a

highly textured manner with the <001> largely oriented in the ND. Groups of these cells or dendrites grow with little to no misorientation between themselves i.e., they solidify as a single grain, with yttria forming in the intercellular or interdendritic regions within the grain.

It has been reported that yttria particles released in a melt are capable of acting as nucleation sites for the BCC β-Ti primary phase during solidification [44]. In order for a nucleant to be efficient, there must normally be a degree of lattice matching to minimise the nucleus-nucleant interfacial energy [60]. This is typically achieved through a semi-coherent interface that requires a specific orientation relationship (OR) [60,66]. Eutectic solidification also often involves a lower energy interface achieved by a habit plane relationship between the two phases [67]. The large area EBSD map shown in Figure 7 provides a large dataset by which to investigate statistically the possibility of an OR between yttria and β-Ti. Further analysis of this data was therefore carried out using MTEX, an open source texture analysis package in Matlab [68]. Figure 10a depicts pole figures for the yttria, the α-Ti and reconstructed β-Ti matrix, all of which show quite strong textures. Due to the large grain size relative to the high resolution EBSD map area, the β-Ti texture is dominated by one main β grain with a weaker second grain rotated relative to it by about 45°. By comparison of these figures, it is notable that there is some obvious alignment between the phases, for example many of the Y_2O_3 {110} poles are closely aligned with those found in the β_{BCC} {111} poles.

After reconstruction of the β-phase orientations, the yttria phase was reassembled with the β-phase data and the combined dataset was analysed using 'calcGrains' to first establish the location of the yttria - β grain boundaries. The reconstructed β grains and yttria particle orientations were subsequently used to calculate Y_2O_3 - β_{BCC} interface minimum-misorientation angle relative-frequency profiles, as shown in Figure **10**b. This plot was constructed, taking into account symmetry, to show the frequency of minimum misorientation angle pairs relative to a direct epitaxial relation. A random misorientation distribution profile, used as a comparison, is also shown in Figure **10**b that was generated in MTEX by superimposing "Random" β orientations on the parent β-phase dataset. The use of random β orientations produces the expected MacKenzian distribution with a peak at 45° [69]. In comparison, the experimental Y_2O_3 - β_{BCC} misorientation distributions have distinct peaks at 30°, 35°, and 45°. These discrete peaks in the misorientation frequency distribution suggest that the yttria particles have formed with a preferred texture that is related to that of β grains, governed by at least one OR. While this statistical analysis is useful to confirm the presence of an OR, it does not provide sufficient information to determine them directly, as multiple ORs may have equivalent minimum misorientation angles (e.g. both the Pitsch and Nishiyama-Wasserman ORs have minimum misorientation angles of 45.98°, but each involves different planes and directions).

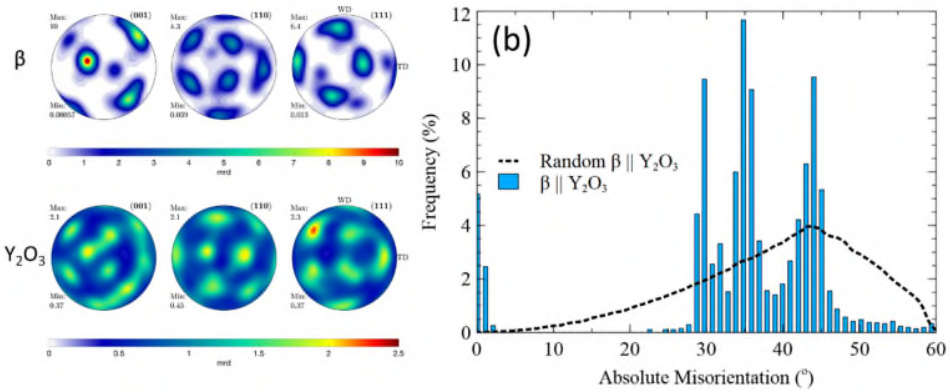

Figure 10: (a) Pole figures from the orientation maps shown in Figure 7, and (b) the resultant calculated misorientation frequency distribution, showing the deviation of the yttria particles from β epitaxy in the both experimental orientation data and with theoretical random β distribution.

Using the so called edge-to-edge matching (E2E) model, Zhang et al. [44] have suggested a $[010]_{\beta}(002)_{\beta}//[110]_{yttria}(004)_{yttria}$ OR between β-Ti and yttria should be favoured. This corresponds to a 45° angular misorientation, with an atomic spacing misfit of 13.9% along the directions, and the interplanar spacings of the $\{002\}_{\beta}$ and $\{004\}_{yttria}$ do not match well as interplanar spacing is not considered in the E2E model. An alternative OR would be with the same $<010>_{\beta}//<110>_{yttria}$ directions in the $\{001\}_{\beta}//\{011\}_{yttria}$ planes which by coincidence have a 13.9% interplanar mismatch. The high likelihood of an OR existing with this pair of planes is reflected in the experimental pole figures (Figure **10**a) which clearly share related pole positions with high intensity. Wang et al. [46] have further proposed a $<111>_{\beta}\{0\bar{1}1\}_{\beta}//<110>_{yttria}\{1\bar{1}0)\}_{yttria}$ β-Ti and Yttria OR with a 6% mismatch; corresponding to a 35.3° angular misorientation. However, this OR requires higher multiples of the lattice spacings to be considered and ignores the repetition of the $\{011\}_{yttria}$ plane at the d/2 position, further complicating the multiplication matching of the Yttria and β lattices, to 4_{yttria}~ 6_{β}. Each of these ORs individually can also only account for single peaks in the misorientation distribution, which was found experimentally to have peaks at 30°, 35° and 45° (Figure **10**b), and neither account for the 30° misorientation.

In order to further explore the most probable ORs between the yttria and Ti-β phases, crystal models of both yttria [70] and β [71] were constructed using the database "Materials Project" [72], and their lattice parameters thermally expanded (detailed in yttria [73], β [26]) in recognition of the high temperatures present during solidification (taken here to be 1600 °C) and evaluated using the software package VESTA for crystal visualization. The low index <001>, <011>, <111>, <120>, <112>, and <221> directions were all considered for potential ORs, by comparing each direction between yttria and β, and as the yttria unit cell is much larger than for β, multiples of the interatomic spacings were also considered. The minimum angular misorientation between directions which had a mismatch below 15% (the assumed partial interface coherency cut-off [60,66]) were then evaluated for their match to the 30°, 35°, and 45° peaks seen in the experimental misorientation plot, Figure **10**b. The interplanar spacings were also considered in the same manner as the directions. Table 3 shows the final 8 most probable ORs determined, which consists of directions that have < 15% mismatch fit in the respective interface planes.

Table 3: β // Y_2O_3 Orientation Relations

Planes		Directions		Mismatch				
				Interplanar		Interatomic		
β	Y_2O_3	β	Y_2O_3	d	(%)	d	(%)	Angular (°)
{001}	{011}	<100>	<112>	$\mathbf{1}_{\beta} \cong \mathbf{1}_{Y_2O_3}$	13.9	$\mathbf{2}_{\beta} \cong \mathbf{1}_{Y_2O_3}$	1.3	35.3
		<011>	<100>			$\mathbf{1}_{\beta} \cong \mathbf{1}_{Y_2O_3}$	13.9	45.0
		<100>	<011>			$\mathbf{1}_{\beta} \cong \mathbf{1}_{Y_2O_3}$	13.9	45.0
{011}	{001}	<112>	<011>	$\mathbf{2}_{\beta} \cong \mathbf{1}_{Y_2O_3}$	13.9	$\mathbf{1}_{\beta} \cong \mathbf{2}_{Y_2O_3}$	7.0	30.0
		<011>	<100>			$\mathbf{1}_{\beta} \cong \mathbf{1}_{Y_2O_3}$	13.9	45.0
		<100>	<011>			$\mathbf{1}_{\beta} \cong \mathbf{1}_{Y_2O_3}$	13.9	45.0
{111}	{011}	<112>	<011>	$\mathbf{2}_{\beta} \cong \mathbf{1}_{Y_2O_3}$	1.3	$\mathbf{1}_{\beta} \cong \mathbf{2}_{Y_2O_3}$	7.0	30.0
		<011>	<100>			$\mathbf{1}_{\beta} \cong \mathbf{1}_{Y_2O_3}$	13.9	45.0

From this analysis it can be concluded that the 'best fit' which has the lowest inter-planar misfit of 1.3% is associated with a {111}β//{011}Y_2O_3; <112> β//<011> β// β//OR, but this alone can only account for the 30° peak. Indeed, it is not possible to explain the 3 peaks in Fig. 10b, without the yittria particles having more than one OR with β. The other 2 ORs cannot be uniquely distinguished using this statistical analysis method, but several candidates with similar misfits are possible from Table 1. Therefore, it seems probable that more than one preferred OR exists between the yttria particles and the β phase, that can be rationalised on the basis of minimisation of the lattice mismatch. However, given how the statistical EBSD data was obtained, any ORs seen here would have formed during (probably eutectic) cooperative nucleation and growth between β and yttria in the inter-dendritic liquid, rather than from a rarer event where a β primary grain nucleated heterogeneously on a yttria particle. Nevertheless, the confirmation of an OR during solidification is indicative of the yttria particles released in to the melt pool during remelting being able to act as nucleants for new β grain orientations if there is sufficient undercooling [44,46].

Finally, a less positive aspect of the refinement trials was that the yttria particles were frequently found to be associated with small pores that are not normally seen in the WAAM process with a standard Ti64 alloy [55]. The change in solidification behaviour due to the addition of Y, that leads to an improved grain structure by providing a larger melting point range and a wider mushy zone with more developed dendrites, will also unfortunately cause a greater gas concentration in the inter-dendritic liquid [74]. Oxide particles are further known to aid nucleation of gas pores within melts [75] and shrinkage porosity will equally be promoted by there being a larger pressure drop from poor liquid feeding in the wider mushy zone in the Y doped solidifying melt pool, through the thin inter-dendritic channels produced by the low partition coefficient of Y when using low addition levels. For example, the images in Figure 5 suggest that liquid feeding through such narrow channels is being blocked during the latter stages of solidification by the formation of the Y_2O_3 particles.

6.0 CONCLUSIONS

Due to its very low partition coefficient with Ti, Y was investigated as a potential alloying addition that could be used at low levels (< 1 wt%) to refine the coarse β grain size normally seen during high deposition rate wire-arc AM of Ti64. It is acknowledged that a relatively simple

experimental method was employed to test this hypothesis that is not suitable for building components, where ideally Y would be incorporated into the feed wire. Nevertheless, the experiments have revealed some interesting insights into the potential for this approach, as well as some disadvantages.

The addition of Y was shown to produce a large reduction in the scale of the coarse-columnar primary β grains that normally develop during solidification under WAAM conditions, but Y did not result in an equiaxed grain structure throughout the build. Although the CET was seen to be crossed where the most favourable solidification conditions were produced (i.e. at the centreline-top of the melt-pool) this refined region was remelted during depositing subsequent layers, resulting in only a finer bulk columnar microstructure.

The Y additions were found to produce yttria particles by scavenging oxygen from the enriched inter-dendritic liquid during the latter stages of solidification. The particles themselves were found to have complex 3D branched morphologies, which when sectioned (in 2D) appeared to be small separate particles. The addition of Y, and the associated development of Y_2O_3 particles within the inter-dendritic channels was also found to have the unwanted side effect of promoting shrinkage porosity in the samples.

It is postulated that the highly-stable yttria particles formed within the inter-dendritic liquid can provide a source of inoculation, by being released into the melt pool during remelting the previous deposited layer. Based on an analysis of the EBSD results, formerly proposed ORs between β and yttria were determined to not individually adequately describe the statistical crystallographic misorientations seen experimentally between the two phases. Several further potential ORs between β and yttria were noted by considering the interatomic mismatches between the two lattices, and it was shown that the misorientation distribution was consistent with more than one OR being operative during the formation of the inter-dendritic yttria particles.

ACKNOWLEDGEMENTS

The authors are appreciative of the EPSRC programme grant NEWAM (EP/R027218/1) and the Innovate UK project Open Architecture Additive Manufacturing (OAAM - WP6) for supporting aspects of this research. The authors acknowledge the use of equipment associated with the Advanced Metals Processing and Characterisation themes of the Henry Royce Institute for Advanced Materials, funded through EPSRC grants EP/R00661X/1, EP/S019367/1, EP/P025021/1 and EP/P025498/1. E.J. Pickering also acknowledges the same grants for funding his position at the Institute. P.B. Prangnell is grateful to the Royal Academy of Engineering, UK, and Airbus for supporting his research through the Airbus-University of Manchester Centre for Metallurgical Excellence.

REFERENCES

[1] G. Welsch, R. Boyer, E.W. Collings, Materials Properties Handbook: Titanium Alloys, ASM International, 1993.

[2] G. Lütjering, J.C. Williams, Titanium, Springer Science & Business Media, 2007.

[3] A. Shokrani, I. Al-Samarrai, S.T. Newman, Hybrid cryogenic MQL for improving tool life in machining of Ti-6Al-4V titanium alloy, J. Manuf. Process. 43 (2019) 229–243. https://doi.org/10.1016/j.jmapro.2019.05.006.
[4] T. Duda, L.V. Raghavan, 3D Metal Printing Technology, IFAC-Pap. 49 (2016) 103–110. https://doi.org/10.1016/j.ifacol.2016.11.111.
[5] W.J. Sames, F.A. List, S. Pannala, R.R. Dehoff, S.S. Babu, The metallurgy and processing science of metal additive manufacturing, Int. Mater. Rev. 61 (2016) 315–360. https://doi.org/10.1080/09506608.2015.1116649.
[6] A.Y. Alfaify, J. Hughes, K. Ridgway, Critical evaluation of the pulsed selective laser melting process when fabricating Ti64 parts using a range of particle size distributions, Addit. Manuf. 19 (2018) 197–204. https://doi.org/10.1016/j.addma.2017.12.003.
[7] G. Nicoletto, R. Konečná, M. Frkáň, E. Riva, Surface roughness and directional fatigue behavior of as-built EBM and DMLS Ti6Al4V, Int. J. Fatigue. 116 (2018) 140–148. https://doi.org/10.1016/j.ijfatigue.2018.06.011.
[8] H. Zhao, A. Ho, A. Davis, A. Antonysamy, P. Prangnell, Automated image mapping and quantification of microstructure heterogeneity in additive manufactured Ti6Al4V, Mater. Charact. 147 (2019) 131–145. https://doi.org/10.1016/j.matchar.2018.10.027.
[9] G. Marinelli, F. Martina, S. Ganguly, S. Williams, Development of Wire + Arc additive manufacture for the production of large-scale unalloyed tungsten components, Int. J. Refract. Met. Hard Mater. 82 (2019) 329–335. https://doi.org/10.1016/j.ijrmhm.2019.05.009.
[10] F. Martina, J. Mehnen, S.W. Williams, P. Colegrove, F. Wang, Investigation of the benefits of plasma deposition for the additive layer manufacture of Ti–6Al–4V, J. Mater. Process. Technol. 212 (2012) 1377–1386. https://doi.org/10.1016/j.jmatprotec.2012.02.002.
[11] A. Ayed, A. Valencia, G. Bras, H. Bernard, P. Michaud, Y. Balcaen, J. Alexis, Effects of WAAM Process Parameters on Metallurgical and Mechanical Properties of Ti-6Al-4V Deposits, in: F. Chaari, M. Barkallah, A. Bouguecha, B. Zouari, M.T. Khabou, M. Kchaou, M. Haddar (Eds.), Adv. Mater. Mech. Manuf., Springer International Publishing, Cham, 2020: pp. 26–35. https://doi.org/10.1007/978-3-030-24247-3_4.
[12] S.A. David, J.M. Vitek, Correlation between solidification parameters and weld microstructures, Int. Mater. Rev. 34 (1989) 213–245. https://doi.org/10.1179/imr.1989.34.1.213.
[13] S.A. David, S.S. Babu, J.M. Vitek, Welding: Solidification and microstructure, JOM. 55 (2003) 14–20. https://doi.org/10.1007/s11837-003-0134-7.
[14] S.W. Williams, F. Martina, A.C. Addison, J. Ding, G. Pardal, P. Colegrove, Wire + Arc Additive Manufacturing, Mater. Sci. Technol. 32 (2016) 641–647. https://doi.org/10.1179/1743284715Y.0000000073.
[15] P.A. Colegrove, A.R. McAndrew, J. Ding, F. Martina, P. Kurzynski, S. Williams, System Architectures for Large Scale Wire + Arc Additive Manufacture, in: tokyo, japan, 2016: p. 5.
[16] P.S.W. Davies, An investigation of microstructure and texture evolution in the Near-α titanium alloy timetal 834., in: 2009.
[17] A.K. Syed, X. Zhang, A.E. Davis, J.R. Kennedy, F. Martina, J. Ding, S. Williams, P.B. Prangnell, Effect of deposition strategies on fatigue crack growth behaviour of wire + arc additive manufactured titanium alloy Ti–6Al–4V, Mater. Sci. Eng. A. 814 (2021) 141194. https://doi.org/10.1016/j.msea.2021.141194.

[18] F. Martina, P.A. Colegrove, S.W. Williams, J. Meyer, Microstructure of Interpass Rolled Wire + Arc Additive Manufacturing Ti-6Al-4V Components, Metall. Mater. Trans. A. 46 (2015) 6103–6118. https://doi.org/10.1007/s11661-015-3172-1.
[19] J.R. Hönnige, P. Colegrove, S. Williams, Improvement of microstructure and mechanical properties in Wire + Arc Additively Manufactured Ti-6Al-4V with Machine Hammer Peening, Procedia Eng. 216 (2017) 8–17. https://doi.org/10.1016/j.proeng.2018.02.083.
[20] J.R. Hönnige, A.E. Davis, A. Ho, J.R. Kennedy, L. Neto, P. Prangnell, S. Williams, The Effectiveness of Grain Refinement by Machine Hammer Peening in High Deposition Rate Wire-Arc AM Ti-6Al-4V, Metall. Mater. Trans. A. (2020). https://doi.org/10.1007/s11661-020-05781-6.
[21] I. Maxwell, A. Hellawell, A simple model for grain refinement during solidification, Acta Metall. 23 (1975) 229–237. https://doi.org/10.1016/0001-6160(75)90188-1.
[22] M. Liu, S. Liu, W. Chen, C. Chen, Y. Lv, X. Zhang, P. Lei, Y. Lin, K. Zhou, Effect of trace lanthanum hexaboride on the phase, grain structure, and texture of electron beam melted Ti-6Al-4V, Addit. Manuf. 30 (2019) 100873. https://doi.org/10.1016/j.addma.2019.100873.
[23] M.J. Bermingham, S.D. McDonald, M.S. Dargusch, Effect of trace lanthanum hexaboride and boron additions on microstructure, tensile properties and anisotropy of Ti-6Al-4V produced by additive manufacturing, Mater. Sci. Eng. A. 719 (2018) 1–11. https://doi.org/10.1016/j.msea.2018.02.012.
[24] Y. Chen, C. Yang, C. Fan, Y. Zhuo, S. Lin, C. Chen, Grain refinement of additive manufactured Ti-6.5Al-3.5Mo-1.5Zr-0.3Si titanium alloy by the addition of La2O3, Mater. Lett. 275 (2020) 128170. https://doi.org/10.1016/j.matlet.2020.128170.
[25] M.J. Bermingham, D.H. StJohn, J. Krynen, S. Tedman-Jones, M.S. Dargusch, Promoting the columnar to equiaxed transition and grain refinement of titanium alloys during additive manufacturing, Acta Mater. 168 (2019) 261–274. https://doi.org/10.1016/j.actamat.2019.02.020.
[26] J.R. Kennedy, A.E. Davis, A.E. Caballero, S. Williams, E.J. Pickering, P.B. Prangnell, The potential for grain refinement of Wire-Arc Additive Manufactured (WAAM) Ti-6Al-4V by ZrN and TiN inoculation, Addit. Manuf. 40 (2021) 101928. https://doi.org/10.1016/j.addma.2021.101928.
[27] Z.X. Du, S.L. Xiao, P.X. Wang, L.J. Xu, Y.Y. Chen, H.K.S. Rahoma, Effects of trace TiB and TiC on microstructure and tensile properties of β titanium alloy, Mater. Sci. Eng. A. 596 (2014) 71–79. https://doi.org/10.1016/j.msea.2013.12.043.
[28] W. Kurz, D.J. Fisher, Fundamentals of solidification, 3. rev. ed., reprinted, Trans Tech Publ, Aedermannsdorf, 1992.
[29] B.J. Spencer, H.E. Huppert, The relationship between dendrite tip characteristics and dendrite spacings in alloy directional solidification, J. Cryst. Growth. 200 (1999) 287–296. https://doi.org/10.1016/S0022-0248(99)00016-0.
[30] S. Ghosh, L. Ma, N. Ofori-Opoku, J.E. Guyer, On the primary spacing and microsegregation of cellular dendrites in laser deposited Ni–Nb alloys, Model. Simul. Mater. Sci. Eng. 25 (2017) 065002. https://doi.org/10.1088/1361-651X/aa7369.
[31] M.J. Bermingham, S.D. McDonald, D.H. StJohn, M.S. Dargusch, Beryllium as a grain refiner in titanium alloys, J. Alloys Compd. 481 (2009) L20–L23. https://doi.org/10.1016/j.jallcom.2009.03.016.
[32] H. Men, Z. Fan, Effects of solute content on grain refinement in an isothermal melt, Acta Mater. 59 (2011) 2704–2712. https://doi.org/10.1016/j.actamat.2011.01.008.

[33] J. Zollinger, M. Escot, L. Deillon, B. Rouat, D. Daloz, T. Dupuy, The role of solute diffusion and temperature on the interface microstructure formation of dissimilar Fe/Fe-Mn-C steels resistance spot welded joints, (n.d.) 10.
[34] D. Shu, B. Sun, J. Mi, P.S. Grant, A quantitative study of solute diffusion field effects on heterogeneous nucleation and the grain size of alloys, Acta Mater. 59 (2011) 2135–2144. https://doi.org/10.1016/j.actamat.2010.12.014.
[35] M. Rappaz, P.H. Thévoz, Solute diffusion model for equiaxed dendritic growth: Analytical solution, Acta Metall. 35 (1987) 2929–2933. https://doi.org/10.1016/0001-6160(87)90292-6.
[36] A.L. Greer, A.M. Bunn, A. Tronche, P.V. Evans, D.J. Bristow, Modelling of inoculation of metallic melts: application to grain refinement of aluminium by Al–Ti–B, Acta Mater. 48 (2000) 2823–2835. https://doi.org/10.1016/S1359-6454(00)00094-X.
[37] S. Roy, S. Suwas, S. Tamirisakandala, D.B. Miracle, R. Srinivasan, Development of solidification microstructure in boron-modified alloy Ti–6Al–4V–0.1B, Acta Mater. 59 (2011) 5494–5510. https://doi.org/10.1016/j.actamat.2011.05.023.
[38] S. Mereddy, M.J. Bermingham, D.H. StJohn, M.S. Dargusch, Grain refinement of wire arc additively manufactured titanium by the addition of silicon, J. Alloys Compd. 695 (2017) 2097–2103. https://doi.org/10.1016/j.jallcom.2016.11.049.
[39] J.H. Luan, Z.B. Jiao, G. Chen, C.T. Liu, Effects of boron additions and solutionizing treatments on microstructures and ductility of forged Ti–6Al–4V alloys, J. Alloys Compd. 624 (2015) 170–178. https://doi.org/10.1016/j.jallcom.2014.11.008.
[40] M. Simonelli, D.G. McCartney, P. Barriobero-Vila, N.T. Aboulkhair, Y.Y. Tse, A. Clare, R. Hague, The Influence of Iron in Minimizing the Microstructural Anisotropy of Ti-6Al-4V Produced by Laser Powder-Bed Fusion, Metall. Mater. Trans. A. 51 (2020) 2444–2459. https://doi.org/10.1007/s11661-020-05692-6.
[41] H.A. Wriedt, J.L. Murray, Binary alloy phase diagrams. Vol. 3., ASM, 1986.
[42] D.W. Bare, E.D. Gibson, O.N. Carlson, TENSILE PROPERTIES OF YTTRIUM-TITANIUM AND YTTRIUM-ZIRCONIUM ALLOYS, 1960. https://doi.org/10.2172/4097762.
[43] M.C. Nordin, G.R. Edwards, D.L. Olson, The Influence of Yttrium Microadditions on Titanium Weld Metal Cracking Susceptibility and Grain Morphology, (n.d.) 11.
[44] D. Zhang, D. Qiu, M.A. Gibson, Y. Zheng, H.L. Fraser, A. Prasad, D.H. StJohn, M.A. Easton, Refining prior-β grains of Ti–6Al–4V alloy through yttrium addition, J. Alloys Compd. 841 (2020) 155733. https://doi.org/10.1016/j.jallcom.2020.155733.
[45] S.M.L. Sastry, J.E. O'neal, R.J. Lederch, B.B. Rath, The effect of yttrium and erbium dispersoids on the deformation behaviour of titanium, J. Mater. Sci. 14 (1979) 179–183. https://doi.org/10.1007/BF01028342.
[46] X. Wang, L.-J. Zhang, J. Ning, S. Li, L.-L. Zhang, J. Long, Hierarchical grain refinement during the laser additive manufacturing of Ti-6Al-4V alloys by the addition of micron-sized refractory particles, Addit. Manuf. 45 (2021) 102045. https://doi.org/10.1016/j.addma.2021.102045.
[47] A. Li, S. Ma, Y. Yang, S. Zhou, L. Shi, M. Liu, Microstructure and mechanical properties of Y2O3 reinforced Ti6Al4V composites fabricated by spark plasma sintering, J. Alloys Compd. 768 (2018) 49–56. https://doi.org/10.1016/j.jallcom.2018.07.229.
[48] Y. Liu, Y. Liu, B. Wang, J. Qiu, B. Liu, H. Tang, Microstructures Evolution and Mechanical Properties of a Powder Metallurgical Titanium Alloy with Yttrium Addition, Mater. Manuf. Process. 25 (2010) 735–739. https://doi.org/10.1080/10426910903365778.

[49] H. Wu, Y. Han, X. Chen, Effects of Yttrium on Mechanical Properties and Microstructures of Ti-Si Eutectic Alloy, Chin. J. Aeronaut. 18 (2005) 171–174. https://doi.org/10.1016/S1000-9361(11)60324-5.
[50] G.C. Obasi, R.J. Moat, D.G. Leo Prakash, W. Kockelmann, J. Quinta da Fonseca, M. Preuss, In situ neutron diffraction study of texture evolution and variant selection during the α→β→α phase transformation in Ti–6Al–4V, Acta Mater. 60 (2012) 7169–7182. https://doi.org/10.1016/j.actamat.2012.09.026.
[51] A.E. Davis, J.R. Kennedy, J. Ding, P.B. Prangnell, The effect of processing parameters on rapid-heating β recrystallization in inter-pass deformed Ti-6Al-4V wire-arc additive manufacturing, Mater. Charact. 163 (2020) 110298. https://doi.org/10.1016/j.matchar.2020.110298.
[52] J.R. Kennedy, A.E. Davis, A. Caballero, A. Garner, J. Donoghue, S. Williams, J. Zollinger, E. Bouzy, E.J. Pickering, P.B. Prangnell, Isomorphic grain inoculation in Ti-6Al-4V during additive manufacturing, Mater. Lett. X. 8 (2020) 100057. https://doi.org/10.1016/j.mlblux.2020.100057.
[53] P.S. Davies, B.P. Wynne, W.M. Rainforth, M.J. Thomas, P.L. Threadgill, Development of Microstructure and Crystallographic Texture during Stationary Shoulder Friction Stir Welding of Ti-6Al-4V, Metall. Mater. Trans. A. 42 (2011) 2278–2289. https://doi.org/10.1007/s11661-011-0606-2.
[54] A. Ho, H. Zhao, J.W. Fellowes, F. Martina, A.E. Davis, P.B. Prangnell, On the origin of microstructural banding in Ti-6Al4V wire-arc based high deposition rate additive manufacturing, Acta Mater. 166 (2019) 306–323. https://doi.org/10.1016/j.actamat.2018.12.038.
[55] J.R. Hönnige, P.A. Colegrove, B. Ahmad, M.E. Fitzpatrick, S. Ganguly, T.L. Lee, S.W. Williams, Residual stress and texture control in Ti-6Al-4V wire + arc additively manufactured intersections by stress relief and rolling, Mater. Des. 150 (2018) 193–205. https://doi.org/10.1016/j.matdes.2018.03.065.
[56] R. Biswal, X. Zhang, A.K. Syed, M. Awd, J. Ding, F. Walther, S. Williams, Criticality of porosity defects on the fatigue performance of wire + arc additive manufactured titanium alloy, Int. J. Fatigue. 122 (2019) 208–217. https://doi.org/10.1016/j.ijfatigue.2019.01.017.
[57] M.J. Bermingham, S.D. McDonald, M.S. Dargusch, D.H. StJohn, Grain-refinement mechanisms in titanium alloys, J. Mater. Res. 23 (2008) 97–104. https://doi.org/10.1557/JMR.2008.0002.
[58] Z. Zou, M. Simonelli, J. Katrib, G. Dimitrakis, R. Hague, Refinement of the grain structure of additive manufactured titanium alloys via epitaxial recrystallization enabled by rapid heat treatment, Scr. Mater. 180 (2020) 66–70. https://doi.org/10.1016/j.scriptamat.2020.01.027.
[59] J. Donoghue, A.E. Davis, C.S. Daniel, A. Garner, F. Martina, J. Quinta da Fonseca, P.B. Prangnell, On the observation of annealing twins during simulating β-grain refinement in Ti–6Al–4V high deposition rate AM with in-process deformation, Acta Mater. 186 (2020) 229–241. https://doi.org/10.1016/j.actamat.2020.01.009.
[60] J.A. Dantzig, M. Rappaz, Solidification, EPFL Press, 2009.
[61] X. Bai, P. Colegrove, J. Ding, X. Zhou, C. Diao, P. Bridgeman, J. roman Hönnige, H. Zhang, S. Williams, Numerical analysis of heat transfer and fluid flow in multilayer deposition of PAW-based wire and arc additive manufacturing, Int. J. Heat Mass Transf. 124 (2018) 504–516. https://doi.org/10.1016/j.ijheatmasstransfer.2018.03.085.

[62] Numerical analysis of heat transfer and fluid flow in multilayer deposition of PAW-based wire and arc additive manufacturing - ScienceDirect, (n.d.). https://www-sciencedirect-com.manchester.idm.oclc.org/science/article/pii/S0017931017352201?via%3Dihub (accessed October 6, 2020).
[63] A.E. Davis, C.I. Breheny, J. Fellowes, U. Nwankpa, F. Martina, J. Ding, T. Machry, P.B. Prangnell, Mechanical performance and microstructural characterisation of titanium alloy-alloy composites built by wire-arc additive manufacture, Mater. Sci. Eng. A. 765 (2019) 138289. https://doi.org/10.1016/j.msea.2019.138289.
[64] J.R. Kennedy, A.E. Davis, A.E. Caballero, M. White, J. Fellowes, E.J. Pickering, P.B. Prangnell, Microstructure Transition Gradients in Titanium Dissimilar Alloy (Ti-5Al-5V-5Mo-3Cr / Ti-6Al-4V) Tailored Wire-Arc Additively Manufactured Components, Mater. Charact. (n.d.).
[65] X. Zhu, H. Yang, X. Dong, S. Ji, The effects of varying Mg and Si levels on the microstructural inhomogeneity and eutectic Mg2Si morphology in die-cast Al–Mg–Si alloys, J. Mater. Sci. 54 (2019) 5773–5787. https://doi.org/10.1007/s10853-018-03198-6.
[66] D.A. Porter, K.E. Easterling, Phase transformations in metals and alloys, 2. ed., reprint, Chapman & Hall, London, 1997.
[67] S.J. Wang, G. Liu, J. Wang, A. Misra, Characteristic orientation relationships in nanoscale Al-Al2Cu Eutectic, Mater. Charact. 142 (2018) 170–178. https://doi.org/10.1016/j.matchar.2018.05.037.
[68] F. Bachmann, R. Hielscher, H. Schaeben, Texture Analysis with MTEX – Free and Open Source Software Toolbox, Solid State Phenom. 160 (2010) 63–68. https://doi.org/10.4028/www.scientific.net/SSP.160.63.
[69] J.K. Mason, C.A. Schuh, The generalized Mackenzie distribution: Disorientation angle distributions for arbitrary textures, Acta Mater. 57 (2009) 4186–4197. https://doi.org/10.1016/j.actamat.2009.05.016.
[70] M.G. Paton, E.N. Maslen, A refinement of the crystal structure of yttria, Acta Crystallogr. 11948-231967. 19 (1965) 307–310.
[71] W.G. Burgers, F.M. Jacobs, Crystal structure of beta-titanium, Z. Fuer Krist. Krist. Krist. Krist. -1441977. 94 (1936) 299–300.
[72] A. Jain, S.P. Ong, G. Hautier, W. Chen, W.D. Richards, S. Dacek, S. Cholia, D. Gunter, D. Skinner, G. Ceder, K. a. Persson, Commentary: The Materials Project: A materials genome approach to accelerating materials innovation, APL Mater. 1 (2013) 011002. https://doi.org/10.1063/1.4812323.
[73] D.W. Stacy, Thermal expansion of the sesquioxides of yttrium, scandium, and gadolinium, Master of Science, Iowa State University, Digital Repository, 1967. https://doi.org/10.31274/rtd-180813-7242.
[74] M.L.N.M. Melo, E.M.S. Rizzo, R.G. Santos, Predicting dendrite arm spacing and their effect on microporosity formation in directionally solidified Al-Cu alloy, J. Mater. Sci. 40 (2005) 1599–1609. https://doi.org/10.1007/s10853-005-0659-y.
[75] A. Samuel, Y. Zedan, H. Doty, V. Songmene, F.H. Samuel, A Review Study on the Main Sources of Porosity in Al-Si Cast Alloys, Adv. Mater. Sci. Eng. 2021 (2021) e1921603. https://doi.org/10.1155/2021/1921603.